Materials Science & Engineering A xxx (xxxx) xxx

Contents lists available at ScienceDirect

Materials Science & Engineering A

journal homepage: http://www.elsevier.com/locate/msea

Mechanical behavior, deformation mechanism and microstructure evolutions of ultrafine-grained Al during recovery via annealing

Y.H. Zhao [a,*], J.F. Bingert [b], T.D. Topping [c], P.L. Sun [d], X.Z. Liao [e], Y.T. Zhu [a,f], E.J. Lavernia [g]

[a] Nano and Heterogeneous Materials Center, School of Materials Science and Engineering, Nanjing University of Science and Technology, Nanjing, 210094, China
[b] Materials Science and Technology Division, Los Alamos National Laboratory, Los Alamos, NM, 87545, USA
[c] Department of Mechanical Engineering, California State University, Sacramento, CA, USA
[d] Department of Materials Science and Engineering, Feng Chia University, Taichung, 40724, Taiwan
[e] School of Aerospace, Mechanical & Mechatronic Engineering, The University of Sydney, Sydney, NSW, 2006, Australia
[f] Department of Materials Science & Engineering, North Carolina State University, Raleigh, NC, 27695-7919, USA
[g] Department of Materials Science and Engineering, University of California, Irvine, CA, 92697, USA

ARTICLE INFO

Keywords:
Ultrafine grained al
Annealing
Mechanical properties
Microstructures
Grain boundary sliding

ABSTRACT

Ultrafine grained (UFG) metals and alloys typically exhibit mechanical and thermal instabilities, partially due to the high density of lattice defects, which limits their engineering applications. Annealing represents a simple and effective way to regain strain hardening, ductility and thermal stability, and stabilize the UFG structures. In this study, we systematically investigated the mechanical behavior, microstructural evolution, fracture and deformation mechanisms of UFG Al during recovery via low-temperature annealing. More specifically we report that low-temperature annealing at 250 °C for 20 min increased the ultimate tensile strength by 10% from 190 to 208 MPa and tensile ductility by 50% from 4.5 to 6.8% without any changes in yield strength (180 MPa). Microstructural analyses indicate that the annealing increased the average grain size from 740 to 840 nm, dislocation density decreased from 5×10^{14} m^{-2} to 1×10^{14} m^{-2}, while the nature of the grain boundaries and associated precipitated phases remained unchanged. Moreover, annealing led to modification of statistically stored dislocations into low-energy dislocation walls (sub-grain boundaries). Results from the fracture surface morphology indicated that the enhanced ductility of the annealed sample was related to the activation of numerous homogeneous micro shear bands, which were controlled by cooperative grain boundary sliding. These observations suggest that the dislocation walls formed during recovery promoted the formation of micro shear bands/cooperative grain boundary sliding and thereby enhanced the ductility.

1. Introduction

Over the past few decades, bulk nanostructured (NS) and ultrafine grained (UFG) metals and alloys have attracted considerable attention, partially due to interesting scientific issues related to their mechanical behavior and deformation mechanisms. From an engineering perspective, the high strength of bulk NS and UFG materials is resulted from high density of lattice defects such as grain boundaries (GBs), triple junctions and dislocations, which are typically 5–10 times higher than those of conventional materials of similar composition, leading to interesting possibilities related to structural applications [1]. However, inspection of the scientific literature reveals that high strength is often achieved at the expense of ductility [2,3] and thermal stability [4–6]. In fact, the reported mechanical (e.g., premature necking) and thermal instabilities (e.g., grain coarsening) are considered to be the major roadblocks that limit the widespread applications of NS materials. In response to these challenges, various strategies and techniques have been proposed and investigated in an effort to address the issues of low ductility [2,7–11] and thermal stability [12–19], with each technique having its own advantages and limitations. Among these techniques, annealing is perhaps the simplest and most widely applicable approach for improving ductility, especially for NS and UFG materials processed by severe plastic deformation (SPD) [20,21]. SPD processed materials typically have high dislocation densities and non-equilibrium GBs [1], making annealing an obvious approach for modifying their microstructures and mechanical behavior.

Inspection of the literature indicates that annealing NS and UFG materials results in the following four trends in strength and ductility: (i)

* Corresponding author.
E-mail address: yhzhao@njust.edu.cn (Y.H. Zhao).

https://doi.org/10.1016/j.msea.2019.138706
Received 23 October 2019; Received in revised form 17 November 2019; Accepted 18 November 2019
Available online 21 November 2019

increasing both strength and ductility [22–27], (ii) increasing ductility by sacrificing strength [28–38], (iii) increasing strength with loss of ductility [39], and (iv) decreasing both strength and ductility [40]. Examples of case (i) can be found in age-hardened NS alloys such as 6061 Al [23], 7075 Al [24], 2219 Al [25], 2024 Al [26], Cu–Cr–Zr alloys [27]. Annealing engineered high-density second-phase precipitates into NS and UFG matrix and lowered dislocation density. The second-phase precipitates resulted in strength increase, and both the second-phase precipitates and the dislocation density reduction resulted in increase in strain hardening capability and ductility. In addition, Valiev et al. [22] reported that low-temperature annealing led to increases in both strength and ductility in commercially pure (CP) NS Ti. After annealing at 300 °C for 10 min, the yield strength of NS Ti was increased by 30% from 800 to 1040 MPa and the ductility was increased from 12% to 21%. The authors attributed the ductility increase to annealing-induced defect ordering at non-equilibrium GBs, which was argued to enhance GB sliding [22]. Examples for the case (ii) have been documented for single-phase NS metals and alloys, such as CP Al [28], 5754 and 5083 Al–Mg alloy [29–31], Cu [32–36], Ni [37], and ferrite/cementite steel [38]. In these materials, annealing gradually decreased strength and increased ductility by introducing microstructural recovery, recrystallization and grain growth. An example of case (iii) was reported for NS CP Al prepared by accumulative rolling bonding (ARB) process [39]. In this study, annealing at 150 °C for 30 min increased the yield strength from 259 to 281 MPa and decreased the ductility from 7 to 1.8%. The authors argued that annealing induced reduction in the generation and interactions of dislocations. Finally, an example of case (iv) was reported for electrodeposited NS Ni sample [40]. In this study, annealing decreased both strength and ductility. The decrease in ductility of the electrodeposited Ni (which had a bimodal grain size distribution) was attributed to the segregation of S and P impurities to GBs, which caused GB de-cohesion and interfacial embrittlement.

From an engineering standpoint, case (i) represents the best-case scenario; however, available results are limited to age-hardened NS alloys. In the case of single-phase NS and UFG metals and alloys, examples of case (ii) are more common. As mentioned above, there is one specific example, that is, case (i) was achieved in single-phase UFG CP Ti [22]. UFG CP Ti exhibits increase in both strength and ductility via low-temperature annealing [22]. However, it is evident that an in-depth understanding of the deformation mechanisms that are responsible for such a phenomenon remains to be established.

For conventional CG materials, GB sliding, as a high-temperature diffusion-controlled deformation process, usually occur when homologous temperature (T/T_m, T_m is the melting point) is larger than 0.5. It is reasonable to anticipate that room temperature may be too low for the occurrence of any significant sliding in NS and UFG materials. Examples of case (iii) and case (iv) behavior might be related to the specific synthesis methods that introduced impurities during material preparation. The impurity segregation to GBs during annealing might result in the observed strength and ductility changes. In one example of case (iii) behavior, the dramatic ductility decrease in UFG Al was attributed to a decrease in dislocation density [39]; however, this argument contradicts the general trend associated with case (ii). In a recent work by Zhao et al. [41], it was reported that lower dislocation density favors the ductility of the pure UFG Cu with clean GBs prepared by high pressure torsion (HPT). However, it is important to note that in this case the UFG Cu sample with higher ductility also contained a larger fraction of high-angle GBs, which complicated the analysis.

In view of the above discussion, the objectives of the present study are threefold. First, to further confirm the simultaneous increase in strength and ductility by annealing (case (i)) in single-phase NS materials. Second, to provide fundamental insight into the underlying origin of the microstructural and deformation mechanisms that governs such behavior. Third, to clarify the influences of dislocation density and configuration on the ductility of UFG metals. In this work, we selected 1050 Al alloy as our model materials given that there have been numerous published studies on UFG 1050 Al. In addition, we selected equal-channel angular pressing (ECAP) as a preparation method to avoid the introduction of impurities and to generate GBs that are relatively free of impurities.

2. Experimental materials and procedures

2.1. Sample preparation

Commercially pure (99.5 wt%) 1050 Al square bars (12 × 12 mm) were used for ECAP experiments. Chemical analysis indicates that the main alloying elements are Fe and Si, as listed in Table 1.

Al square bars were processed using ECAP at ambient temperature by route A for 8 passes (henceforth designated as the sample A). The ECAP die has an L-shape channel with an intersecting channel angle of 90° and an outer-arc angle of 45°, which imposes an effective strain of approximately 1 per ECAP pass. In route A, the sample was not rotated between adjacent passes. The sample A was then annealed at 250 °C for 20 min (designated as sample A-anneal) under Ar atmosphere.

2.2. Tensile testing

Flat dog-bone tensile specimens with gauge dimensions of 10 × 1 × 2 mm^3 were sectioned by electrical discharge machining (EDM) from the central regions of the UFG 1050 Al bars with the gauge axis parallel to the extrusion direction and the gauge flat surface parallel to top plane of the extrusion bar (e.g., Z plane as defined in Ref. [42]). All tensile specimens were polished before testing using a diamond suspension with particle size of 0.25 μm. Three samples were prepared for each state in order to ensure reproducibility. Uniaxial tensile tests were performed at room temperature on an Instron 8801 universal testing machine (UTM) using Bluehill 2 software with an initial quasi-static strain rate of 10^{-3} s^{-1}. The strain was measured using a standard non-contacting video extensometer with a 100 mm field-of-view lens.

2.3. Microstructure characterization

Microstructures of the Al samples after ECAP and after annealing were characterized using electron backscattered diffraction (EBSD), transmission electron microscopy (TEM), energy-dispersive X-ray spectroscopy (EDX) mapping, X-ray diffraction (XRD), scanning electron microscopy (SEM) and atomic force microscopy (AFM) measurements. The grip sections of the tensile specimens were used for EBSD, TEM, EDX and XRD examinations. TEM observation was carried out on a Philips CM12 microscope operated at 100 kV. To prepare TEM specimens, the grip sections of the tensile specimens were polished into thin foils with thicknesses of about 50 μm. The thin foils were twin-jet electro-polished by a solution of 25 vol% nitric acid +75 vol% Methanol for 2 min at a voltage of 15 V and a temperature of 238 K. The EDX mapping was performed on a JOEL 2500 transmission electron microscope operating at 200 kV.

Quantitative EBSD measurements were carried out on a TSL OIM system on a Philips XL30 FEG SEM with step sizes of 50–150 nm. Boundary structures of the two samples are analyzed using EBSD. Quantitative XRD measurements were performed on a Scintag X-ray diffractometer equipped with a Cu target operating at 1.8 kW to estimate the dislocation density. The θ-2θ scans were conducted at room temperature at a scan speed of 1°/min. Pure aluminum annealed at 673 K

Table 1
Chemical compositions of the as-received AA1050 Al alloy analyzed in Luvak Inc. (Boylston, MA). The analysis method is direct current plasma emission spectroscopy – ASTME – 1097-03. The main alloying elements are Fe and Si.

Wt.%	Si	Fe	Cu	Mn	Mg	Zn	Ti	Al
Luvak Inc.	0.08	0.31	0.003	0.036	0.004	0.009	0.008	99.5

was used as an XRD peak-broadening reference for both grain size and microstrain calculations [43–45]. The peak parameters (peak intensity, peak-maximum position, full width at half maximum and integral breadth) were determined by fitting a Pearson VII function to the measured peaks [43–45]. The fracture surface and morphology was imaged by a FEI-XL30 SFEG SEM using a 25 kV beam and a Nanoscope®IIIa Scanning Probe Microscope operating in a tapping mode.

2.4. XRD data evaluation

On the basis of an XRD peak broadening method, the grain size and microstrain as well as dislocation density of the Al samples after ECAP and after annealing were calculated. Specifically, integral width was used to characterize the peak broadening. The measured intensity profile of the Bragg reflection is a convolution of the physical intensity profile with an instrumental broadening profile. The instrumental broadening profile determined by means of coarse-grained Al reference sample is revealed as to be a Gaussian type [43]. The measured profile of the Bragg reflection in the Al samples A and A-anneal possesses primarily a Lorentzian component. By supposing that the physical profiles of the Al samples A and A-anneal are primarily a Lorentzian type, the physical intensity profile can be separated by removing the instrumental broadening effect from the measured intensity profile. The physical broadening profile can be considered as the convolution of the grain-size broadening profile (usually represented by a Lorentzian function [46]) with that of the microstrain broadening (a Gaussian function [47]). Then from the integral width of the physical broadening profile, the grain size and the microstrain of the sample can be calculated in terms of the Scherrer and Wilson equation [47]:

$$\frac{\beta_{hkl}^2}{tg^2\theta_{hkl}} = \frac{\lambda\beta_{hkl}}{D_{hkl}tg\theta_{hkl}\sin\theta_{hkl}} + 16 < \varepsilon_{hkl}^2 >^{1/2}, \quad (1)$$

where D_{hkl} and $< \varepsilon_{hkl}^2 >^{1/2}$ represent the thickness and the mean magnitude of microstrain of the grains in the $<hkl>$ direction, respectively. λ is the wavelength of Cu $K_{\alpha 1}$ irradiation. By performing a least-square fit to $\beta_{hkl}^2/tg^2\theta_{hkl}$ plotted against $\lambda\beta_{hkl}/(tg\theta_{hkl}sin\theta_{hkl})$ for all of the measured peaks of the samples, the mean grain size D and the mean microstrain $< \varepsilon^2 >^{1/2}$ can be determined. Standard linear regression techniques provide an estimate for the uncertainty in the parameters from the error in the fit [48]. Dislocations density ρ can be represented in terms of D and $< \varepsilon^2 >^{1/2}$ by Ref. [49]:

$$\rho = 2\sqrt{3} < \varepsilon^2 >^{1/2} \Big/ (D * b), \quad (2)$$

where b is the Burgers vector of dislocations, and equals 0.2863 nm for Al.

Determination of the lattice parameters in Al samples after ECAP and after annealing includes two stages. First, λ_{ka2} component was removed from the XRD profiles by the modified Rachinger method [50,51]. Second, the lattice parameters of the Al samples after ECAP and after annealing were calculated from the intensity peak centroid positions. In order to minimize the system error, the external standard method using a pure Si polycrystal was employed to calibrate the peak positions. The calibration function was:

$$\Delta 2\theta = \alpha + \beta\cos\theta + \gamma\sin\theta, \quad (3)$$

where α relates to 2θ-axis origin displacement, β relates to eccentricity between the sample and goniometer center axis, and γ relates to the sample flatness or absorption.

3. Results

3.1. Mechanical properties

The representative engineering stress–strain curves of the UFG 1050 Al samples A and A-anneal are compared in Fig. 1. It is apparent that sample A has a yield strength value of 180 MPa, and that annealed sample A did not change its yield strength, but evidently increased its ultimate tensile strength by 10% from 190 ± 5 MPa to 208 ± 5 MPa. Necking was evident in both samples shortly after yielding, leading to a dominant post-necking elongation contribution to the elongation to failure. Sample A has a uniform elongation of about 0.9%, and annealing increased this value slightly to 1.4%. After the onset of necking, the reduction in the stress versus strain curve (strain-hardening rate) in the sample A-anneal was slower than that in sample A, resulting in a larger elongation to failure of 6.8 ± 0.5%. The elongation to failure of sample A is 4.5 ± 0.5%.

3.2. Microstructures

3.2.1. Grain size and distribution

Quantitative EBSD results are shown in Figs. 2 and 3 from representative regions of samples A and A-anneal. From Fig. 2, it is apparent that the plastic deformation induced by ECAP in samples A and A-anneal was not uniform, resulting in a mixture of micron and sub-micron sized grains. Moreover, there are numerous fine sub-micron grains (with a size less than 250 nm) distributed at the GBs of micrometer or sub-micrometer grains. The fine sub-micrometer grains are likely to have formed as a result of dynamic recrystallization during ECAP processing and annealing (for sample A-anneal), as verified by TEM results presented in the next section. The above results were further confirmed by the grain size distribution histograms, as shown in Fig. 3(a). Both samples have grain size distributions that can be described as bimodal (i.e., a mixture of fine sub-micron grains and sub-micro/micron grains). Annealing sample A slightly shifted the histogram to a larger grain sizes and reduced its fraction of fine sub-micron grains from 4.0 to 2.5% due to limited grain growth. The grain sizes were determined using a 5° minimum misorientation boundary criterion. The average grain size, calculated as an equivalent diameter derived from area orientation measurements, is 740 nm for sample A and 840 nm for sample A-anneal, as listed in Table 2. The discrete step size used for EBSD mapping based

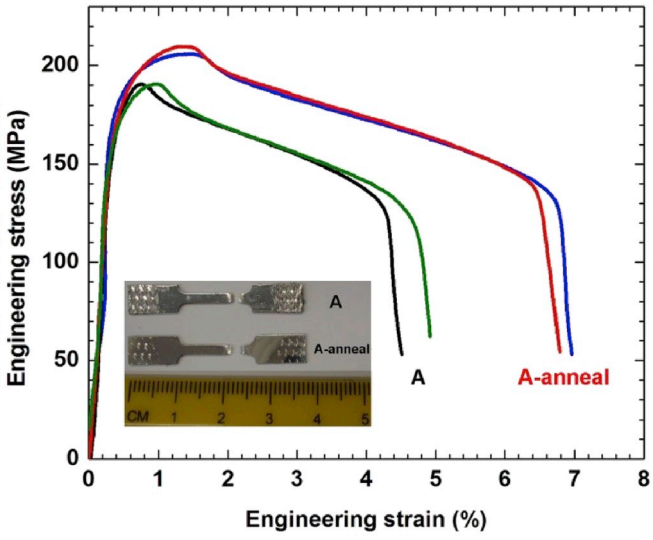

Fig. 1. Tensile engineering stress-strain curves of the UFG AA1050 Al samples A and A-anneal at a strain rate of 10^{-3} s^{-1}. The inset shows fractured tensile specimens with gauge dimensions of 10 mm × 2 mm × 1 mm.

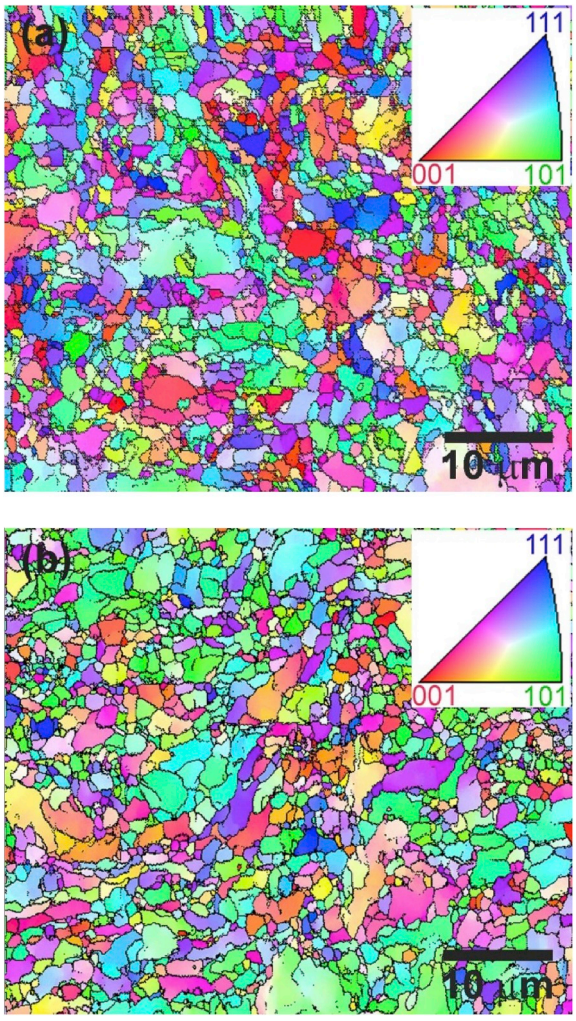

Fig. 2. EBSD crystal orientation maps of the UFG AA1050 Al samples A (a) and A-anneal (b).

the statistics against any remnant grains smaller than approximately 150 nm. The grain size calculated from XRD results are 210 ± 20 nm and 250 ± 20 nm for samples A and A-anneal, respectively, which are smaller than those values from EBSD because XRD calculates the sub-grain/domain size. Nevertheless, the grain sizes of samples A and A-anneal are comparable.

3.2.2. Grain boundaries

The GB misorientation angle distributions, determined using EBSD are shown in Fig. 3b. Boundaries with misorientation angles above 15° are generally defined as high-angle GBs (HAGBs), and low-angle GBs (LAGBs) have misorientation angles smaller than 15° [52]. Considering all boundaries with misorientations >2°, sample A has 73% of HAGBs. Annealing sample A did not significantly change its HAGB fraction (75%). The various peaks observed in the sample misorientation angle distributions have three potential sources. First, the deformation texture component developed during the ECAP process may yield preferred misorientations at 35.3°, 35.6°, 43°, 45°, 46°, and 54.7° [53]. Second, there may be pre-existing Σ3 (60°), Σ27a (31.6°), and Σ27b (35.4°) coincident-site lattice (CSL) boundaries that are evolved from the recrystallized twin population and associated boundary reaction networks within the initial microstructure [54]. Third, CSL boundaries may have developed from twin growth related to partial recrystallization during the ECAP deformation. From the insets in Fig. 3(a, b), annealing did not change the pole figure/texture of sample A.

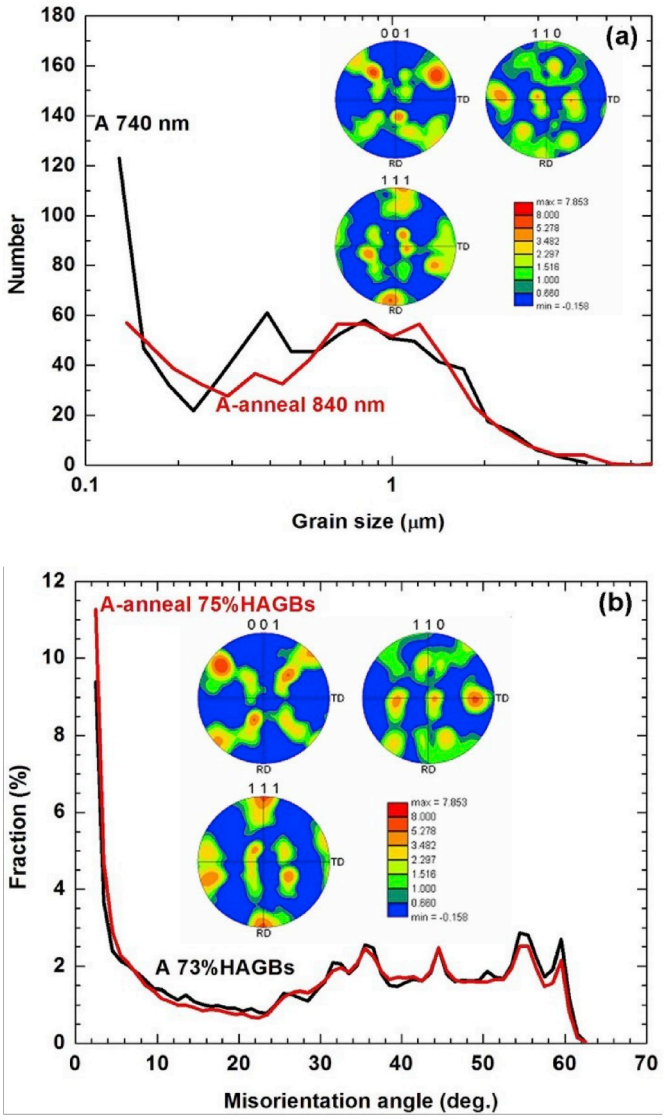

Fig. 3. The grain size (a) and grain boundary misorientation angle (b) distributions of the UFG AA1050 Al samples A and A-anneal measured by EBSD mapping. The insets in (a) and (b) are pole figures of samples A and A-anneal, respectively.

3.2.3. Dislocations

TEM observations indicated that statistically stored dislocations (such as entangled dislocations, dislocation forests and discrete single dislocations) were frequently observed in grains in sample A (marked by white and black arrows in Fig. 4a and b), but rarely in sample A-anneal (Fig. 4c), indicating a much higher statistically stored dislocation density in sample A. In contrast, sub-GBs were readily apparent in sample A-anneal (as pointed by white arrows in Fig. 4c). This result suggests that annealing sample A annihilated the dislocation forests and tangled dislocations via forming sub-GBs within grains. The sub-GBs are revealed as polygonized dislocation walls (PDWs) with low misorientation angles, as shown in Fig. 4d. The wavy and diffuse GBs in sample A and A-anneal were caused by small orientation variations among the grains/sub-grains (Fig. 4a and c).

The microstrain, analyzed by X-ray diffraction (XRD), was 0.87 ± 0.08% and 0.21 ± 0.02% in sample A and A-anneal, respectively. The dislocation densities in sample A and A-anneal, were then calculated as $5.0 \pm 0.5 \times 10^{14}$ m^{-2} and $1.0 \pm 0.2 \times 10^{14}$ m^{-2}, respectively, further confirming the TEM observations. The fine sub-micrometer grains marked by black arrows in Fig. 4c are thought to form as a result of

Table 2
A list of microstructures of samples A and A-anneal: average grain size, D, fraction of fine sub-micron grains, F_{fg}, grain size distribution, D_d, fraction of high-angle GBs, F_{HAGBs}, dislocation density, ρ, dislocation configurations.

Samples	D (nm)	F_{fg} (%)	D_d	F_{HAGBs} (%)	ρ (10^{14} m^{-2})	dislocation configurations
A	740	4.0	Bi-modal	73	5	Statistically stored dislocations
A-anneal	840	2.5	Bi-modal	75	1	Geometrically necessary dislocations

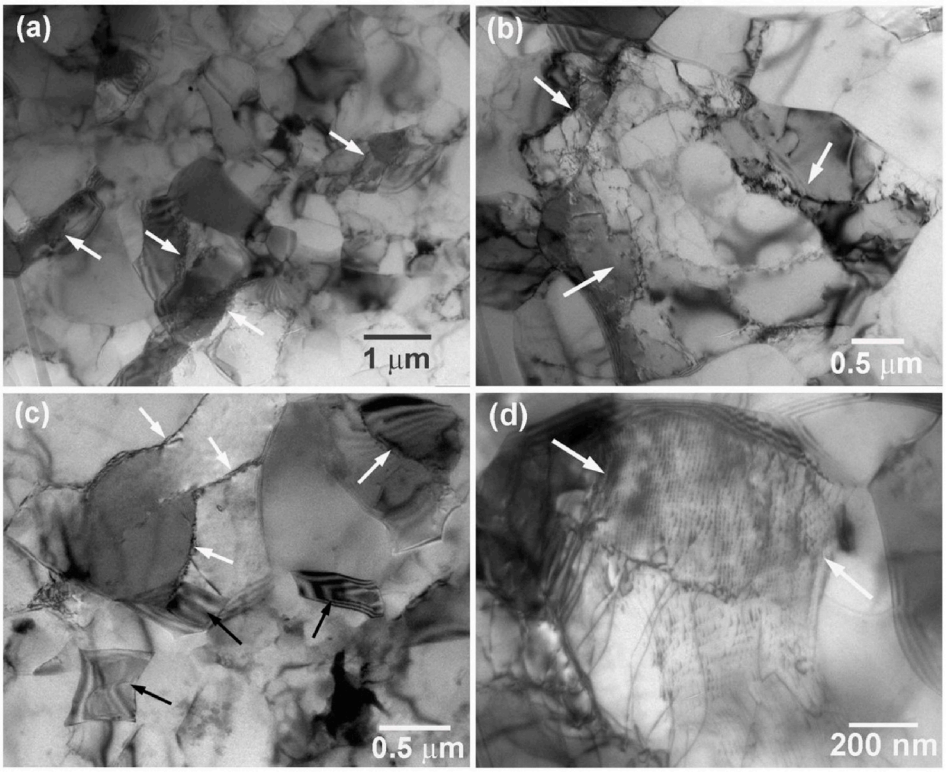

Fig. 4. TEM images of the UFG AA1050 Al samples A (a,b) and A-anneal (c,d). Dislocation forests and tangle in sample A were marked by white arrows in Fig. 4a and b, and discrete single mobile dislocations were marked by black arrows in Fig. 4b. The sub-grain boundaries in sample A-anneal were pointed by white arrows in Fig. 4c. The black arrows in Fig. 4c show the recrystallized fine sub-micron grains. Fig. 4d shows polygonized dislocation walls (PDWs) forming a sub-grain boundary, as pointed by white arrows.

recrystallization due to their large orientation differences from their surrounding matrix.

3.2.4. Solid solution and precipitates

Fe and Si atoms are the primary solutes in the commercial purity Al and their contents are 0.08 Si, 0.31 Fe wt.%, respectively. However, at ambient temperature only small amounts of Si and Fe are soluble in Al: 1.65 wt% for Si and 0.052 wt% for Fe. Therefore, the additional 0.164 wt % Fe will be transformed into 2nd phase precipitates [55,56].

Careful TEM observations revealed the presence of second phase precipitates with a globular morphology that were heterogeneously distributed in the Al matrix of both as-ECAP-processed and annealed samples. However, the density of these precipitates is very low, and the average distance between precipitates is about several tens of micrometers for both samples. EDX mapping indicates that these precipitates are enriched in Fe, Si, and Si and O in both annealed and un-annealed samples, as shown in Figs. 5–9. These precipitates have sizes ranging from several tens of nanometers to several hundreds of nanometers. XRD measurements indicate that these particles are cubic Al_4Si, triclinic $AlSi_2O_{10}$ and cubic $AlFe_3$ second phases, as shown in Fig. 10. Since we used the same areas for XRD scanning for both the annealed and un-annealed samples, the XRD peak intensity of the second phase particles corresponds to their volume fractions. From Fig. 10, it is evident that annealing did not affect the volume fraction of precipitates, at least on the basis of the resolution of XRD. Overall, the amount of second phase particles remained very small in all samples studied. On the basis of XRD results, the annealed and un-annealed samples have Al matrix

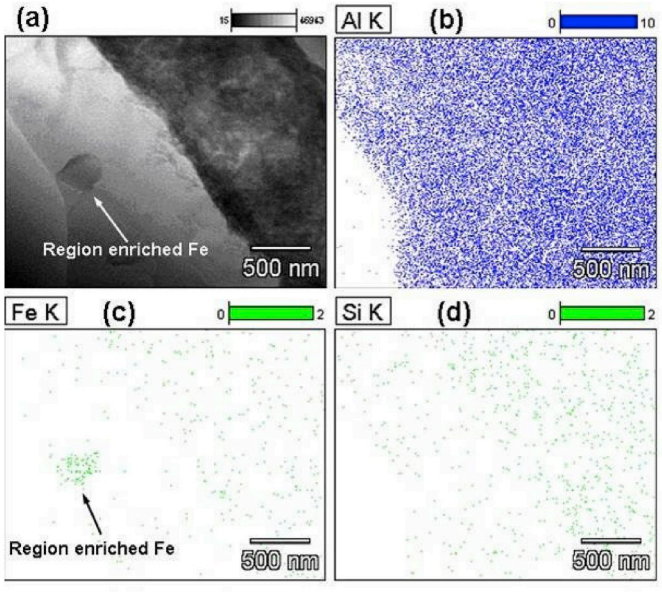

Fig. 5. Energy-dispersive X-ray spectroscopy (EDX) mapping of sample A. (a) Base image of EDX mapping, (b)–(e) EDX mapping of elements Al, Fe, Si. There is a region enriching Fe.

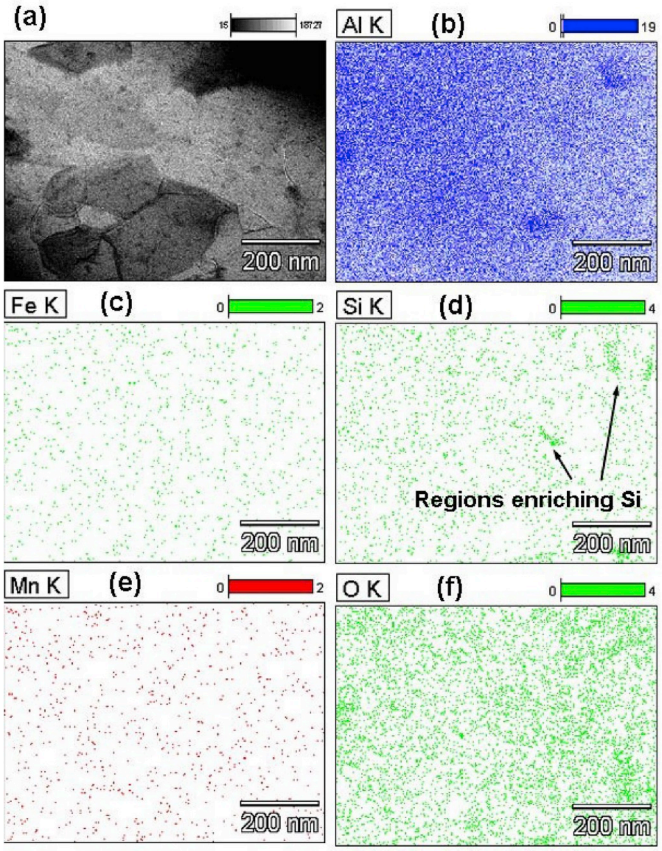

Fig. 6. Energy-dispersive X-ray spectroscopy (EDX) mapping of sample A. (a) Base image of EDX mapping, (b)–(f) EDX mapping of elements Al, Fe, Si, Mn and O. There are regions enriching Si.

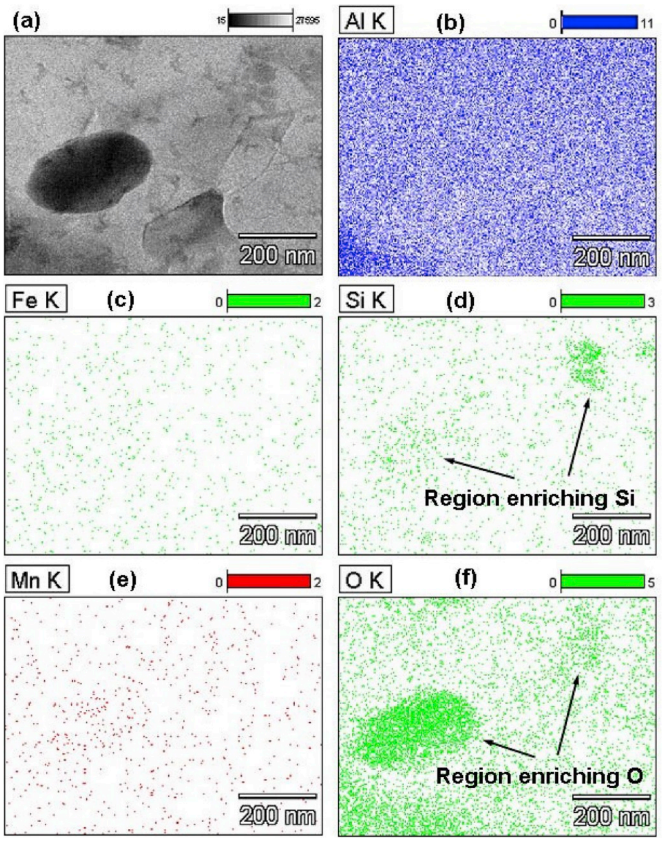

Fig. 7. Energy-dispersive X-ray spectroscopy (EDX) mapping of sample A. (a) Base image of EDX mapping, (b)–(f) EDX mapping of elements Al, Fe, Si, Mn and O. There are regions enriching Si and O.

lattice parameters of 0.4049 ± 0.0002 nm and 0.4045 ± 0.0002 nm, respectively, which are comparable with that of the pure Al (0.4049 ± 0.0002 nm), and may be rationalized on the basis of a solid solution. The fact that both as-ECAP-processed and annealed samples exhibited comparable lattice parameters further confirms the prior observation that a 20 min anneal did not significantly alter either the solid solution or the volume fraction of precipitates. Moreover, energy-dispersive X-ray spectroscopy (EDX) mapping did not find GB segregation prior to and following annealing. These results suggest that the main influence of the annealing step was to promote recovery of the dislocation structure (e.g., reduce dislocation density and alter dislocation configuration), and hence did not result in evident grain growth, texture change, or composition/2nd-phase particle changes.

3.3. Fracture morphologies

To provide insight into mechanical behavior and establish a relationship between microstructures and mechanical properties, we studied the fracture mode and fracture surface morphology using SEM. Fig. 11 shows the SEM images of the macro- and micro-scale fracture surfaces of sample A (a,b) and A-anneal (c,d). Both as-ECAP-processed and annealed Al samples fractured via ductile mechanisms, as verified by their large area reduction of fracture surfaces, *A*, and the numerous dimples over the entire fracture surface. From the macro-scale SEM images in Fig. 11(a) and (c), the fracture surface area reduction was 40.2% and 42.5% for the as-ECAP-processed and annealed Al samples, respectively, as listed in Table 3. The difference of *A* values between the two samples is so small that it falls within measurement error bar. From the micro-scale SEM images in Fig. 11(b) and (d), homogeneously distributed honeycomb-like dimples were observed to range from 1 to about 10 μm. Moreover, the dimples in both samples are elongated due to void nucleation and subsequent coalescence via shear fracture, as verified by the following results. There is no evident difference in the dimples between the as-ECAP-processed and annealed Al samples.

Fig. 12 shows the macro-scale side-view SEM images of the as-ECAP-processed (a) and annealed (b,c) Al samples. Both samples fail in a shear fracture mode with a shear fracture angle θ (the angle between the fracture surface and tension axis) of about 49° for the as-ECAP-processed Al sample and 53° for the annealed Al sample, as listed in Table 3. The shear fracture can be attributed to the nanostructures, which resulted in a decreased ratio of the average critical normal fracture stress to shear fracture stress [57].

3.4. Deformation mechanisms

3.4.1. Observation of deformation via SEM

To further understand the mechanical behavior and fracture mechanisms, we carried out both SEM and AFM to reveal deformation mechanisms of the UFG Al samples. Fig. 13 shows the macro- (a,d) and micro-scale (b,c,e,f) face-view SEM images of the as-ECAP-processed (a-c) and annealed Al samples (d-f). Careful observation on the sample surface revealed numerous localized plastic deformation markings or traces parallel with each other near the fracture edge within the necking zones. Several published studies reported similar deformation traces in UFG Al [58,59], Al6082 alloys [60], Ni [61], and Cu [62], and these were described as microscopic or mesoscopic shear bands or shear planes. The orientations of these shear bands changed gradually from an angle of about 45° to the tensile axis to an angle of 90° from positions close to the sample sides to sample center (Fig. 13b and c, 13d and 13e). The distances between shear bands vary from several micrometers to several tens of micrometers, and the lengths of the shear bands extend

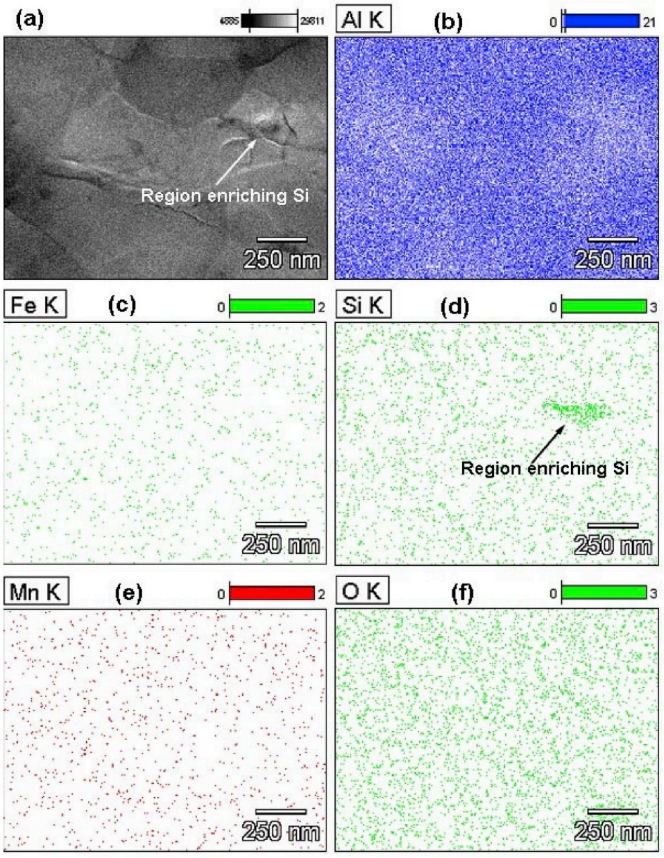

Fig. 8. Energy-dispersive X-ray spectroscopy (EDX) mapping of sample A-anneal. (a) Base image of EDX mapping, (b)–(f) EDX mapping of elements Al, Fe, Si, Mn and O. There is a region enriching Si.

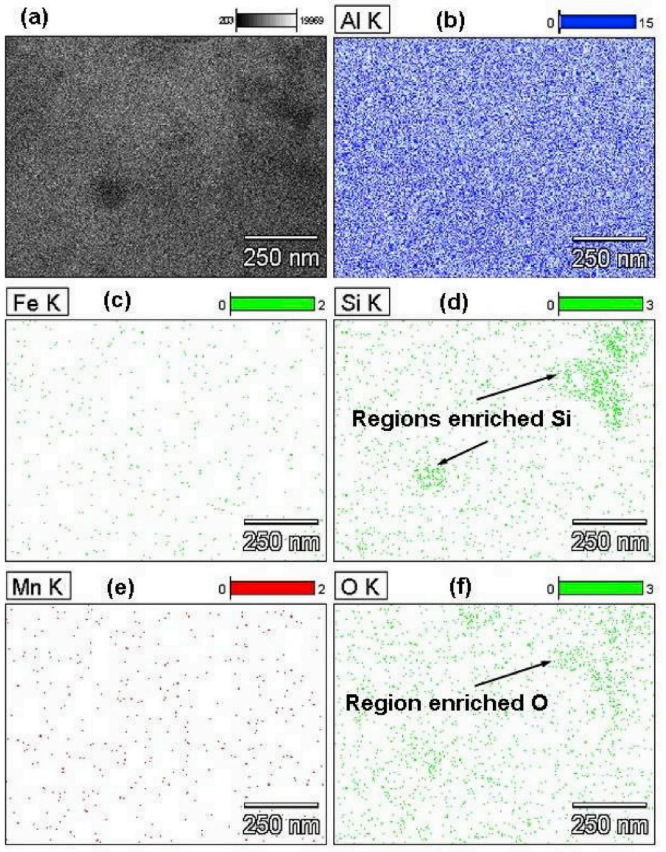

Fig. 9. Energy-dispersive X-ray spectroscopy (EDX) mapping of sample A-anneal. (a) Base image of EDX mapping, (b)–(i) EDX mapping of elements Al, Fe, Si, Mn, O. There are regions enriching Si and O.

from several micrometers to one hundred micrometers. The shear bands disappeared gradually when leaving the necking regions to the uniform deformation regions. By comparing the shear bands of the ECAP-processed and annealed Al samples, one can see the shear bands are much coarser in the as-ECAP-processed Al sample than in the annealed Al sample. This suggests that the formation of the high density of fine shear bands may have enhanced the plastic deformation capability and overall tensile ductility.

The length and distance of the micro shear bands are about several tens of grain size (700–800 nm). It means that localized plastic deformation is not confined to the grain interior and developed on a greater scale and suggests an operative fracture mechanism involving cooperative deformation in multiple grains [62,63], which will be discussed in details in the following discussion part. The above observations also suggest that the annealed microstructures favor the formation of micro shear bands, resulting in the larger post-necking elongation.

3.4.2. *Three-dimensional analysis of the surface by AFM*

To further characterize the nature of the shear bands, AFM analysis was performed. Fig. 14 show representative fragments of the surface tomography from face-view of the deformed and un-deformed as-ECAP-processed and annealed Al samples. Qualitative and quantitative analyses of the AFM images provided results similar to those obtained from the SEM images. The surface of the un-deformed as-ECAP-processed Al is smooth with few scratches with depth of several tens of nanometers introduced by the final polishing process, as shown in Fig. 14(a,b). After tensile deformation, extensive shear bands throughout the necking zone are clearly seen. There appear numerous intruded grooves on the tensile specimen's surface near the fracture edge, as shown in Fig. 14(c–f) for the as-ECAP-processed Al sample. The depth of these grooves could be in

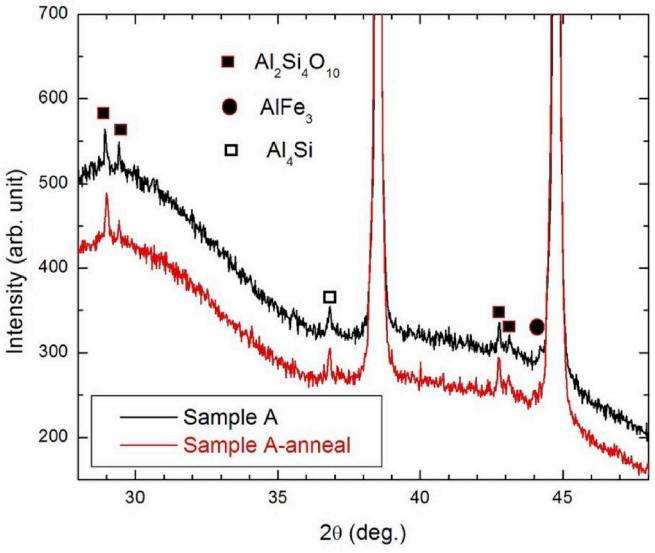

Fig. 10. XRD patterns of samples A and A-anneal. Both samples have cubic Al_4Si, triclinic $AlSi_2O_{10}$ and cubic $AlFe_3$ precipitates. Since we used the same areas for XRD scanning for both annealed and unannealed samples, the XRD peak intensity of the 2nd-phase particles corresponds to their volume fractions. From Fig. 10, after annealing the volume fraction of precipitates was not changed.

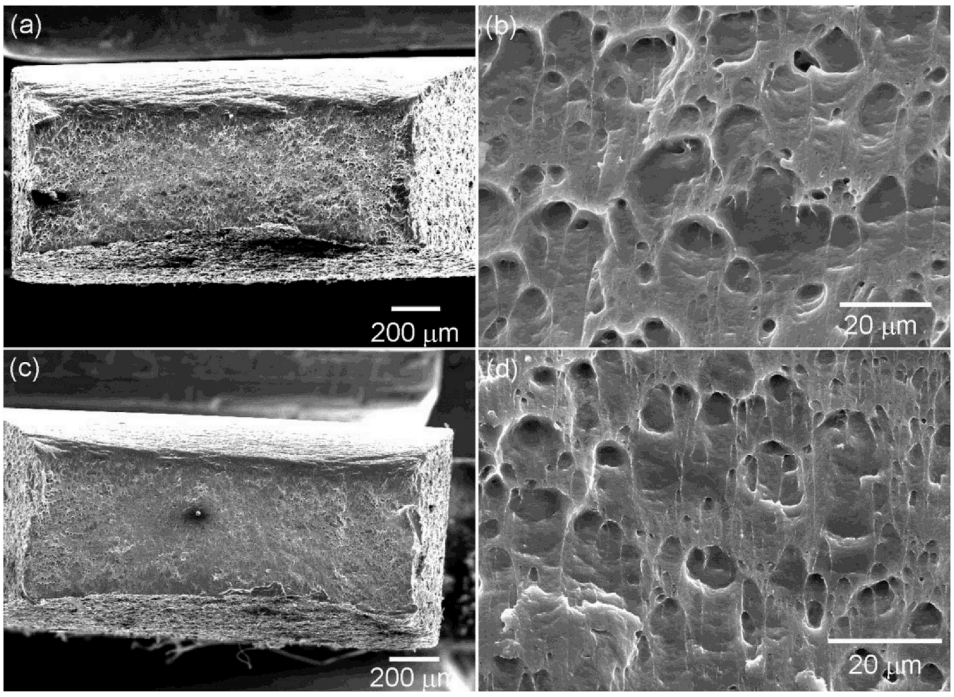

Fig. 11. SEM images of the fracture surfaces of the as-ECAP'ed (a,b) and annealed Al (c,d). (a,c) Lower magnification, (b,d) higher magnification to show dimples.

Table 3
A list of microstructures of samples A and A-anneal: precipitates, area reduction of fracture surface, *A*, shear fracture angle, θ.

Samples	*Precipitates*	*A* (%)	θ (°)
A	Al_4Si, $AlSi_2O_{10}$, $AlFe_3$	40.2	49
A-anneal	Al_4Si, $AlSi_2O_{10}$, $AlFe_3$	42.5	53

micrometer range, and the distance between the neighboring grooves ranges from several micrometers to several tens of micrometers, consistent with the size of shear bands observed by SEM.

In addition, AFM images also revealed many spherical extruded particulates located at the grooves in Fig. 14(e) and (f). These particulates have height of several hundreds of nanometers, and sizes ranging from several hundreds of nanometers to several micrometers, the same size range as the grains. The extruded particulates suggest that there might exist displacements between two adjacent grains along their

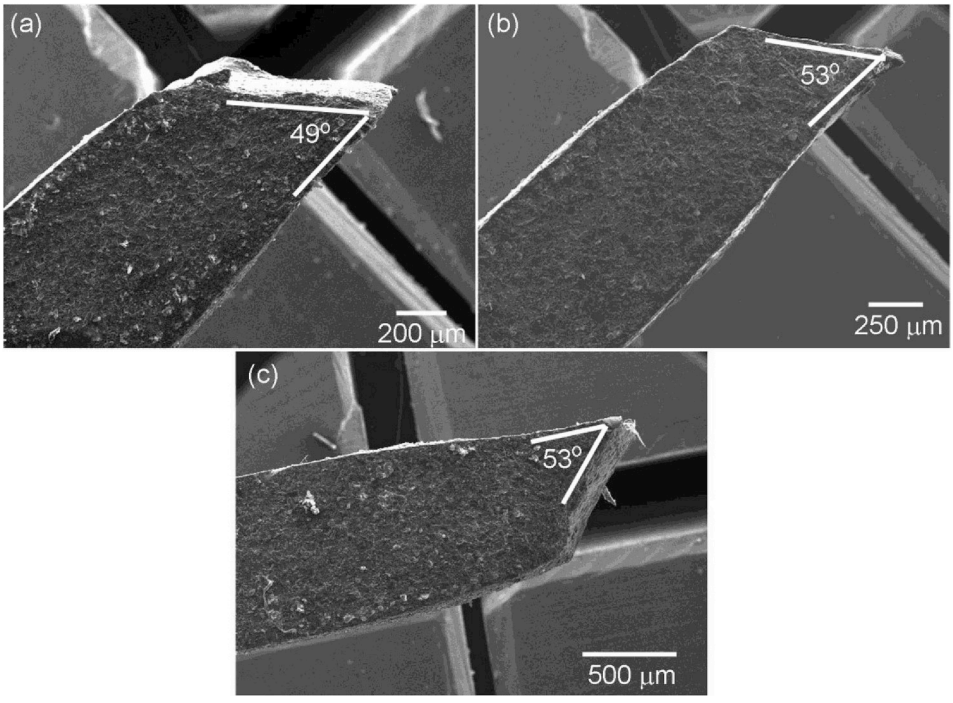

Fig. 12. SEM images from side-view of the as-ECAP'ed Al (a) and annealed Al specimens (b,c) to show shear fracture. Image (c) was obtained from the opposite side of the tensile specimen shown in (b).

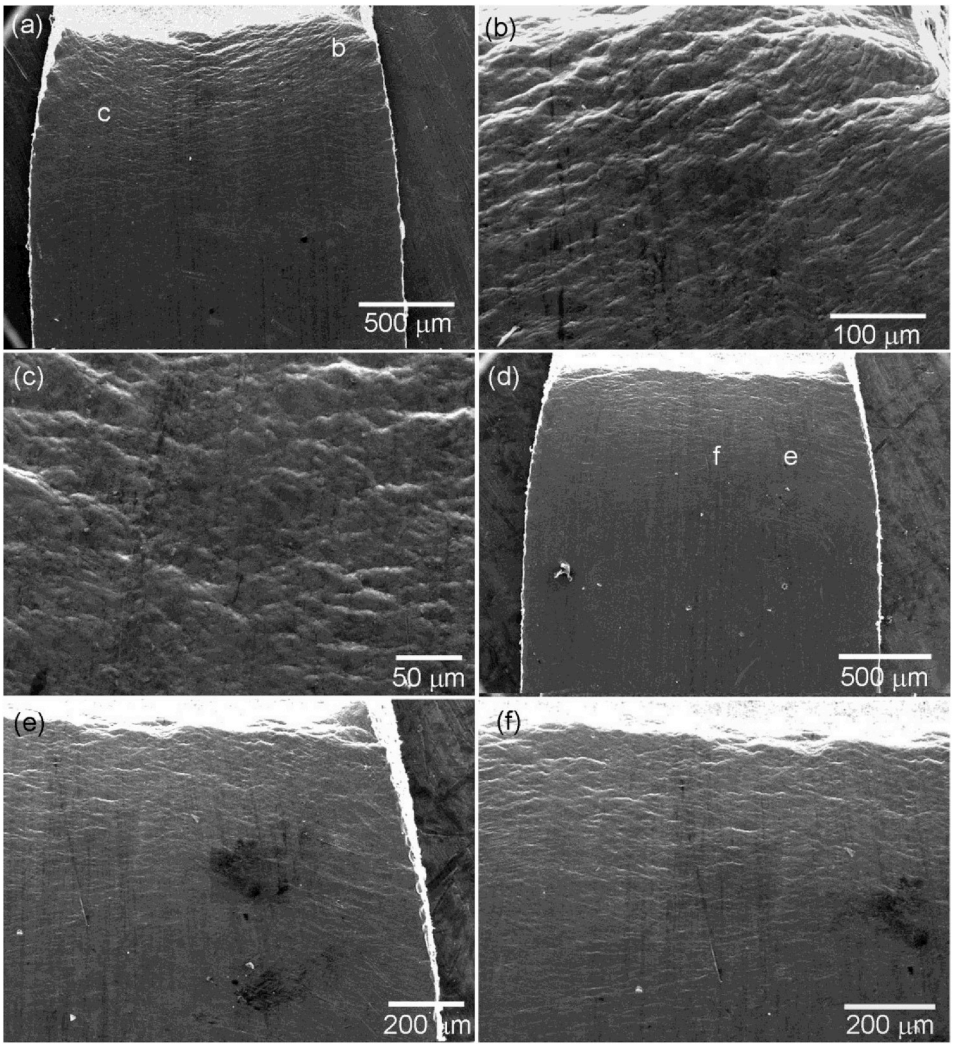

Fig. 13. SEM images from face-view of the as-ECAP'ed Al (a–c) and annealed Al (d–f) to show micro shear bands. (a,d) Lower magnification, (b,c,e,f) higher magnification to show shear bands near specimen sides (b,e) and close to the centers (c,f), respectively for the as-ECAP'ed Al (b,c) and annealed Al (e,f).

boundaries. The mutual GB displacement can be identified as GB sliding, which is an essential mechanism during creep and superplasticity and is particularly effective at elevated temperatures [62,63]. Similar grooves and particulates were also found in the annealed Al sample, as shown in Fig. 14(g and h). The depth of the grooves and neighboring groove distance of the annealed Al are much smaller than that of the as-ECAP-processed Al sample, agreeing with the SEM observations.

4. Discussion

4.1. Microstructure-property relationship

Tables 2 and 3 reveal that annealed sample A significantly lowered its statistically stored dislocation density and slightly increased its average grain size, which are anticipated to decrease the yield strength. However, the above loss in yield strength might be compensated by dislocation configuration changes [39,64], resulting in unchanged yield strength. Annealing transformed statistically stored dislocations into low-energy polygonized dislocation walls (PDWs), and hence a higher stress was needed to activate new dislocations [39,64]. In addition, it is also possible that some impurities diffused to the dislocation cores during the annealing, which will pin the dislocations. GB segregation is a very common phenomenon in UFG/NS materials because of enhanced diffusivity along GBs [65,66], and it has been reported to increase the yield strength of NS Ni–Fe alloys [67]. However, there is no GB segregation detected in the present work and the reasons might be (i) the Si (0.08 wt%) and Fe (0.3 wt%) amounts are too low to detect, or (ii) there is no GB segregation considering Fe and Si formed second phases and the lattice of Al matrix is close to that of pure Al.

The enhancement in ductility and strain hardening by annealing might be rationalized on the basis of two factors. First, the presence of a low density of statistically stored dislocations, or low-energy dislocation configuration, and second, grain growth. The evident strain hardening in the uniform elongation segment of sample A originated from small amount of large micrometer-sized grains (as shown in Fig. 2), which still possess further dislocation accumulation capacity. Annealing sample A further recovered the strain hardening ability of micrometer grains, resulting in evident increase in uniform elongation [28,68]. The dominant post-necking elongation in both samples A and A-anneal was caused by geometrical/localized instability due to insufficient strain hardening/dislocation accumulation capability in UFG grains during tension [28,68]. Annealing resulted in an enhancement in hardening rate and a reduction in dynamic recovery rate of UFG grains by annihilating and stabilizing the statistically stored dislocations and therefore increased the post-necking elongation.

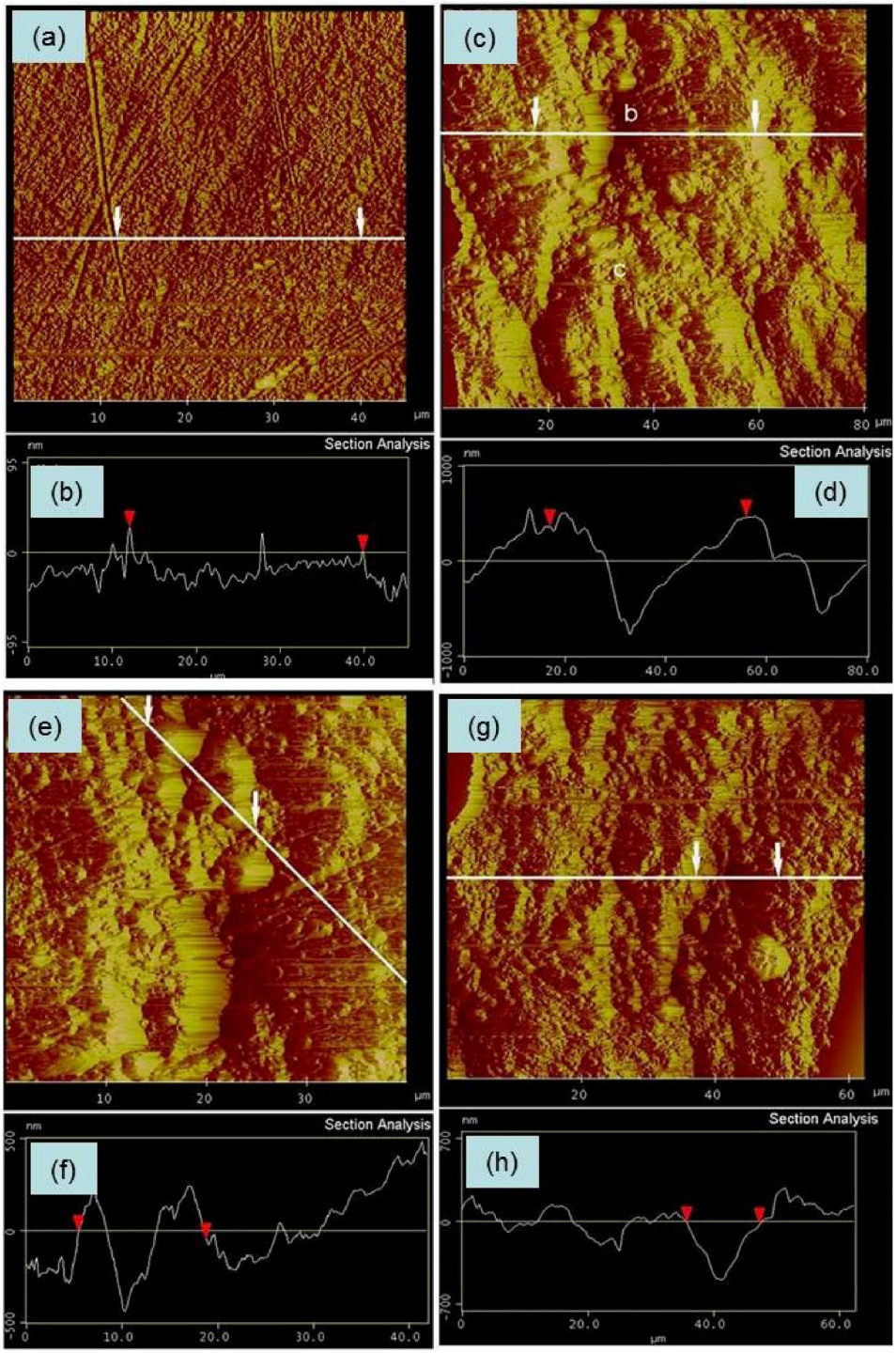

Fig. 14. Three-dimensional AFM image of the surface topographies from face-view of the un-deformed as-ECAP'ed Al sample (a), deformed as-ECAP'ed Al (c,e) and deformed as-annealed Al sample (g) with their corresponding profiles (b,d,f,h).

4.2. Deformation mechanisms

After numerous investigations on the deformation mechanisms of NS and UFG materials via experiments, molecular dynamic (MD) simulations and other modeling efforts in last several decades, the deformation mechanisms of NC and UFG materials have been reported to include GB-mediated deformation such as GB sliding [69–74], grain rotation [75–78], stress-driven GB migration [79–83], GB diffusion [61,63, 84–86], partial dislocations from GBs [87], deformation twinning [88] besides the conventional slip of lattice dislocations [89,90]. As known, the conventional dislocation slip dominates plastic deformation of coarse-grained metals. As a result of GB-mediated deformation, grain growth or coalescence usually occurred [91–93]. Nevertheless, NC and UFG materials have revealed a significant decrease in ductility at room temperature due to decreased strain hardening capability [94]. In the sections that follow, we discuss each one within the context of the results described herein.

4.2.1. Grain boundary sliding

GB sliding is one of the GB-mediated deformation mechanisms and is

a well-established deformation process for CG materials deformed at elevated temperatures [95,96]. During GB sliding, individual grains of a polycrystalline material are displaced with respect to each other along their mutual boundaries as a consequence of an external stress. Without other accommodation mechanisms, GB sliding does not occur in a polycrystalline matrix, thus it follows that the sliding of individual grains must be accommodated either through the diffusional flow of vacancies as in diffusion creep [95,96] or through the intra-granular dislocation slip as in dislocation creep or superplasticity [96].

It has been reported that the GB sliding of NS and UFG materials could occur even at room temperatures [58–62,69–85] due to the following reasons. First, enhanced diffusion kinetics: it has been suggested that diffusion can play an important role in the plastic deformation of NS and UFG metals and alloys, even at room temperature. This is related to the increased volume fraction of GBs, which promotes GB diffusion processes due to enhanced diffusivity [65,66]. This may result in GB sliding at room temperature by atom shuffling and so-called athermal ('stress-induced') GB diffusion [80–83]. Second, NS and UFG materials possess reasonably high fractions of HAGBs and non-equilibrium GBs with many extrinsic dislocations lying in narrow regions adjacent to the GBs [23]. It is probable that these boundaries and the associated high dislocation densities provide easy diffusive paths for the local re-arrangements that are needed to form GB sliding. Thus the presence of these GBs will promote GB sliding provided the temperature is sufficiently high that diffusion-controlled processes can occur rapidly. Third, some in situ TEM observations and MD simulations also revealed stress-driven GB migration [80–83], which is an athermal activation process. This means GB sliding can occur even at very low temperature, and experiments observed GB sliding even at liquid nitrogen temperature [80].

4.2.2. *Cooperative grain boundary sliding and micro shear bands*

Based on GB sliding, a theoretical model for the deformation of NS and UFG materials i.e., formation of mesoscopic glide planes, has been proposed by Hahn et al. [97]. For materials having grain size at the NS and UFG levels, it was argued that the volume of the GBs represents a significant fraction of the overall volume of the material and this provides an opportunity for the formation of long planar inter-faces, stretching over many grains, where localized displacements result in the development of macroscopic sliding over dimensions that are significantly larger than the individual grains. It is noted that only a minor perturbation of the blocking material through localized diffusion leads readily to a mesoscopic planar interface and to sliding over relatively long distances. Moreover, by in situ SEM and TEM observations, Mukherjee et al. found a cooperative GB sliding of UFG materials at ambient and elevated temperatures, which usually controls the superplastic behavior of microcrystalline materials [61,62,84]. Both cooperative GB sliding and mesocopic shear planes are microscopic sliding or shear bands involving a cooperative slide of a series of NS and UFG grains, which are verified by MD and modeling computer simulations [70,98] as well as experiments [58–61,99,100]. Shear bands or localizations as a result of cooperative GB sliding or mesoscopic shear planes have been observed in NC Fe [100], Cu [99] and UFG Al [58,59] and Al 6061 [60], Cu [61], Ni [62] as well as the present results.

It should be noted that the micro shear bands for the UFG metal are different from those seen in CG materials [101,102]. In CG materials, micro shear bands form within a coarse grain, and their initial dimensions are significantly smaller than the (coarse) grain size. These micro shear bands grow by spreading into neighboring grains across GBs and eventually form macro shear bands. Such a relationship between the grain size and the dimensions of micro shear band does not apply to NS and UFG metals. Therefore, those shear bands in UFG metals whose width/grain size ratio fall in the range 1–10 are defined as micro shear bands. Note that this is distinct from macro shear bands which spread across the entire specimen cross-section, forming a fracture surface and resulting in failure.

The present results indicate that the annealed UFG Al has much denser and finer micro shear bands compared with the as-ECAP-processed UFG Al. By comparing the microstructural change during annealing, one may hypothesize that the fine shear bands were promoted by the PDWs formed sub-GBs. As discussed above, these dislocation walls could promote GB sliding by dislocation related diffusion, climb, slip etc. In addition, Valiev et al. [22] observed similar GBs in the annealed UFG Ti and argued that these GBs with dislocations could result in GB sliding which further enhanced the ductility.

5. Conclusions

In summary, low-temperature annealing simultaneously enhanced the ultimate strength and ductility of the UFG AA1050 Al sample with no measureable reduction in yield strength. Comparison of the microstructural changes prior to and after annealing suggests that a low-energy dislocation configuration (geometrically necessary dislocations), low statistically stored dislocation density and slight grain growth are beneficial to a higher ductility of the annealed UFG AA1050 Al. It is also suggested that the reported absence of variations in yield strength with annealing are attributed to the presence of low-energy dislocation configuration and/or impurity segregation to grain boundaries. Results from studies of the fracture surface morphology indicate that the enhanced ductility of the annealed sample was related to the activation of numerous homogeneous micro shear bands, which is controlled by cooperative grain boundary sliding. On the basis of our results and analysis we propose that the dislocation walls formed during recovery promote the formation of micro shear bands/cooperative grain boundary sliding and thereby enhance the tensile ductility.

Author's contribution

Y.H. Zhao did TEM, XRD, AFM, EDX and SEM microstructural and deformation analysis as well as annealing process, and wrote the first draft of the paper; J.F. Bingert did EBSD; T.D. Topping did tensile test, P. L. Sun did ECAP processing; X.Z. Liao, Y.T. Zhu and E.J. Lavernia discussed the results and revised the paper.

Declaration of competing interest

The authors declare that they have no known competing financial interests or personal relationships that could have appeared to influence the work reported in this paper.

Acknowledgments

Y.H. Zhao acknowledges financial supports from the National Key R&D Program of China (Grant No. 2017YFA0204403), National Natural Science Foundation of China (Grant No. 51971112 and 51225102) and the Fundamental Research Funds for the Central Universities (Grant No. 30919011405), The authors would like to acknowledge support by the University of California, Irvine (EJL) and the Australian Research Council.

References

[1] Y. Cao, S. Ni, X.Z. Liao, M. Song, Y.T. Zhu, Structural evolutions of metallic materials processed by severe plastic deformation, Mater. Sci. Eng. R 133 (2018) 1–59.
[2] I.A. Ovid'ko, R.Z. Valiev, Y.T. Zhu, Review on superior strength and enhanced ductility of metallic nanomaterials, Prog. Mater. Sci..94 462-540.
[3] C.C. Koch, D.G. Morris, K. Lu, A. Inoue, Ductility of nanostructured materials, MRS Bull. 24 (1999) 54–58.
[4] Y. Huang, S. Sabbaghianrad, A.I. Almazrouee, K.J. Al-Fadhalah, S.N. Alhajeri, T. G. Langdon, The significance of self-annealing at room temperature in high purity copper processed by high-pressure torsion, Mater. Sci. Eng. A 656 (2016) 55–66.
[5] M. Ames, J. Markmann, R. Karos, A. Michels, A. Tschope, R. Birringer, Unraveling the nature of room temperature grain growth in nanocrystalline materials, Acta Mater. 56 (2008) 4255–4266.

[6] V.Y. Gertsman, R. Birringer, On the room-temperature grain growth in nanocrystalline copper, Scr. Metall. Mater. 30 (1994) 577–581.
[7] C.C. Koch, Optimization of strength and ductility in nanocrystalline and ultrafine grained metals, Scr. Mater. 49 (2003) 657–662.
[8] E. Ma, Instabilities and ductility of nanocrystalline and ultrafine-grained metals, Scr. Mater. 49 (2003) 663–668.
[9] C.C. Koch, K.M. Youssef, R.O. Scattergood, K.L. Murty, Breakthroughs in optimization of mechanical properties of nanostructured metals and alloys, Adv. Eng. Mater. 7 (2005) 787–794.
[10] E. Ma, Eight routes to improve the tensile ductility of bulk nanostructured metals and alloys, J. Occup. Med. 58 (2006) 49–53.
[11] Y.H. Zhao, Y.T. Zhu, E.J. Lavernia, Strategies for improving tensile ductility of bulk nanostructured materials, Adv. Eng. Mater. 12 (2010) 769–778.
[12] X. Zhou, X.Y. Li, K. Lu, Enhanced thermal stability of nanograined metals below a critical grain size, Science 360 (2018) 526–529.
[13] N. Liang, Y.H. Zhao, Q. Zhan, J.F. Bingert, E.J. Lavernia, Stabilizing ultrafine grained Cu by grain lamella, J. Mater. Sci. 53 (2018) 13173–13185.
[14] F. Abdeljawad, S.M. Foiles, Stabilization of nanocrystalline alloys via grain boundary segregation: a diffuse interface model, Acta Mater. 201 (2015) 159–171.
[15] C.C. Koch, R.O. Scattergood, K.A. Darling, J.E. Semones, Stabilization of nanocrystalline grain size by solute additions, J. Mater. Sci. 43 (2008) 7264–7272.
[16] M.A. Atwater, R.O. Scattergood, C.C. Koch, The stabilization of nanocrystalline copper by zirconium, Mater. Sci. Eng. A 559 (2013) 250–256.
[17] X.C. Liu, H.W. Zhang, K. Lu, Strain-induced ultrahard and ultrastable nanolaminated structure in nickel, Science 342 (2013) 337–340.
[18] C. Saldana, T.G. Murthy, M.R. Shankar, E.A. Stach, S. Chandrasekar, Stabilizing nanostructured materials by coherent nanotwins and their grain boundary triple junction drag, Appl. Phys. Lett. 94 (2009), 021910.
[19] L.F. Zeng, R. Gao, Q.F. Fang, X.P. Wang, Z.M. Xie, S. Miao, T. Hao, T. Zhang, High strength and thermal stability of bulk Cu/Ta nanolamellar multilayers fabricated by cross accumulative roll bonding, Acta Mater. 110 (2016) 341–351.
[20] R.Z. Valiev, R.K. Isamgaliev, I.V. Alexandrov, Bulk nanostructured materials from severe plastic deformation, Prog. Mater. Sci. 45 (2000) 103–189.
[21] R.Z. Valiev, Y. Estrin, Z. Horita, T.G. Langdon, M.J. Zehetbauer, Y.T. Zhu, Producing bulk ultrafine-grained materials by severe plastic deformation, J. Occup. Med. 58 (2006) 33–39.
[22] R.Z. Valiev, A.V. Sergueeva, A.K. Mukherjee, The effect of annealing on tensile deformation behavior of nanostructured SPD titanium, Scr. Mater. 49 (2003) 669–674.
[23] J.K. Kim, H.K. Kim, J.W. Park, W.J. Kim, Large enhancement in mechanical properties of the 6061 Al alloys after a single pressing by ECAP, Scr. Mater. 53 (2005) 1207–1211.
[24] Y.H. Zhao, X.Z. Liao, S. Cheng, E. Ma, Y.T. Zhu, Simultaneously increasing the ductility and strength of nanostructured alloys, Adv. Mater. 18 (2006) 2280–2283.
[25] T. Shanmugasundaram, B.S. Murty, V.S. Sarma, Development of ultrafine grained high strength Al–Cu alloy by cryorolling, Scr. Mater. 54 (2006) 2013–2017.
[26] S. Cheng, Y.H. Zhao, Y.T. Zhu, E. Ma, Optimizing the strength and ductility of fine structured 2024 Al alloy by nano-precipitation, Acta Mater. 55 (2007) 5822–5832.
[27] N. Takata, Y. Ohtake, K. Kita, K. Kitagawa, N. Tsuji, Increasing the ductility of ultrafine-grained copper alloy by introducing fine precipitates, Scr. Mater. 60 (2009) 590–593.
[28] C.Y. Yu, P.W. Kao, C.P. Chang, Transition of tensile deformation behaviors in ultrafine-grained aluminum, Acta Mater. 53 (2005) 4019–4028.
[29] H. Jin, D.J. Lloyd, Effect of a duplex grain size on the tensile ductility of an ultra-fine grained Al–Mg alloy AA5754 produced by asymmetric rolling and annealing, Scr. Mater. 50 (2004) 1319–1323.
[30] Z. Horita, K. Ohashi, T. Fujita, K. Kaneko, T.G. Langdon, Achieving high strength and high ductility in precipitation-hardened alloys, Adv. Mater. 17 (2005) 1599–1602.
[31] B.Q. Han, F.A. Mohamed, C.C. Bampton, E.J. Lavernia, Improvement of toughness and ductility of a cryomilled Al-Mg alloy via microstructural modification, Metall. Mater. Trans. A 36 (2005) 2081–2091.
[32] Y.M. Wang, M.W. Chen, F.H. Zhou, E. Ma, High tensile ductility in a nanostructured metal, Nature 419 (2002) 912–915.
[33] E. Rabkin, I. Gutman, M. Kazakevich, E. Buchman, D. Gorni, Correlation between the nanomechanical properties and microstructure of ultrafine-grained copper produced by equal channel angular pressing, Mater. Sci. Eng. A 396 (2005) 11–21.
[34] D. Das, A. Samanta, P.P. Chattopadhyay, Mechanical properties of bulk ultrafine-grained copper, Synthesis and Reactivity in Inorganic, Metal Organic Nano Metal Chem. 36 (2006) 221–225.
[35] C.X. Huang, S.D. Wu, G.Y. Li, S.X. Li, Influences of cyclic deformation and subsequent aging treatment on the tensile properties of Cu processed by equal-channel angular pressing, Mater. Sci. Eng. A 483–484 (2008) 433–436.
[36] Y.S. Li, Y. Zhang, N.R. Tao, K. Lu, Effect of thermal annealing on mechanical properties of a nanostructured copper prepared by means of dynamic plastic deformation, Scr. Mater. 59 (2008) 475–478.
[37] T.R. Lee, C.P. Chang, P.W. Kao, The tensile behavior and deformation microstructure of cryo-rolled and annealed pure nickel, Mater. Sci. Eng. A 408 (2005) 131–135.
[38] M.C. Zhao, F. Yin, T. Hanamura, K. Nagai, A. Atrens, Relationship between yield strength and grain size for a bimodal structural ultrafine-grained ferrite/cementite steel, Scr. Mater. 57 (2007) 857–860.
[39] X.X. Huang, N. Hansen, N. Tsuji, Hardening by annealing and softening by deformation in nanostructured metals, Science 312 (2006) 249–251.
[40] M.J.N.V. Prasad, S. Suwas, A.H. Chokshi, Microstructural evolution and mechanical characteristics in nanocrystalline nickel with a bimodal grain-size distribution, Mater. Sci. Eng. A 503 (2009) 86–91.
[41] Y.H. Zhao, J.F. Bingert, Y.T. Zhu, X.Z. Liao, R.Z. Valiev, Z. Horita, T.G. Langdon, Y.Z. Zhou, E.J. Lavernia, Tougher ultrafine grain Cu via high-angle grain boundaries and low dislocation density, Appl. Phys. Lett. 92 (2008), 081903.
[42] P.L. Sun, E.K. Cerreta, J.F. Bingert, G.T. Gray III, M.F. Hundley, Enhanced tensile ductility through boundary structure engineering in ultrafine-grained aluminum, Mater. Sci. Eng. A 464 (2007) 343–350.
[43] Y.H. Zhao, K. Lu, Grain-size dependence of thermal properties of nanocrystalline elemental selenium studied by x-ray diffraction, Phys. Rev. B 56 (1997) 14330–14337.
[44] Y.H. Zhao, H.W. Sheng, K. Lu, Microstructure evolution and thermal properties in nanocrystalline Fe during mechanical attrition, Acta Mater. 49 (2001) 365–375.
[45] Y.H. Zhao, K. Lu, K. Zhang, Microstructure evolution and thermal properties in nanocrystalline Cu during mechanical attrition, Phys. Rev. B 66 (2002), 085404.
[46] J.I. Langford, R. Delhez, ThH. de Keijser, E.J. Mittemeijer, Profile analysis for microcrystalline properties by the Fourier and other methods, Aust. J. Phys. 41 (1988) 173–187.
[47] H.P. Klug, L.E. Alexander, X-ray Diffraction Procedures for Polycrystalline and Amorphous Materials, second ed., John Wiley and Sons, New York, 1974, pp. 491–662.
[48] P.R. Bevington, Data Reduction and Error Analysis for the Physical Sciences, McGraw-Hill, New York, 1969.
[49] Y.H. Zhao, X.Z. Liao, Z. Jin, R.Z. Valiev, Y.T. Zhu, Microstructure and mechanical properties of ultra-fine grained 7075 Al alloys processed by ECAP and their evolutions during annealing, Acta Mater. 52 (2004) 4589–4599.
[50] J. Labell, A. Zagofsky, S. Pearlman, Cu Kα2 elimination algorithm, J. Appl. Crystallogr. 8 (1975) 499–506.
[51] G. Platbrood, Kα2 elimination algorithm for Cu, Co and Cr radiations, J. Appl. Crystallogr. 16 (1983) 24–27.
[52] D.A. Hughes, N. Hansen, High angle boundaries formed by grain subdivision mechanics, Acta Mater. 45 (1997) 3871–3886.
[53] J.H. Cho, A.D. Rollett, K.H. Oh, Determination of volume fractions of texture components with standard distributions in Euler space, Metall. Mater. Trans. A A35 (2004) 1075–1086.
[54] V. Randle, B. Ralph, D. Dingley, The relationship between microstructure and grain boundary parameters, Acta Metall. 36 (1988) 267–273.
[55] C.M. Allen, K.A.Q. O'Reilly, B. Cantor, P.V. Evans, Intermetallic phase selection in 1XXX Al alloys, Prog. Mater. Sci. 43 (1998) 89–170.
[56] I.S. Lee, P.W. Kao, N.J. Ho, Microstructure and mechanical properties of Al–Fe in situ nanocomposite produced by friction stir processing, Intermetallics 16 (2008) 1104–1108.
[57] Z.F. Zhang, J. Eckert, Unified tensile fracture criterion, Phys. Rev. Lett. 94 (2005), 094301.
[58] Y. Huang, T.G. Langdon, Using atomic force microscopy to evaluate the development of mesoscopic shear planes in materials processed by severe plastic deformation, Mater. Sci. Eng. A 358 (2003) 114–121.
[59] N.Q. Chinh, P. Szommer, Z. Horita, T.G. Langdon, Experimental evidence for grain-boundary sliding in ultrafine-grained aluminum processed by severe plastic deformation, Adv. Mater. 18 (2006) 34–39.
[60] I. Sabirov, Y. Estrin, M.R. Barnett, I. Timokhina, P.D. Hodgson, Tensile deformation of an ultrafine-grained aluminium alloy: micro shear banding and grain boundary sliding, Acta Mater. 56 (2008) 2223–2230.
[61] A. Vinogradov, S. Hashimoto, V. Patlan, K. Kitagawa, Atomic force microscopic study on surface morphology of ultra-fine grained materials after tensile testing, Mater. Sci. Eng. A 319–323 (2001) 862–866.
[62] A.V. Sergueeva, N.A. Mara, A.K. Mukherjee, Plasticity at really diminished length scales, Mater. Sci. Eng. A 463 (2007) 8–13.
[63] A.V. Sergueeva, N.A. Mara, N.A. Krasilnikov, R.Z. Valiev, A.K. Mukherjee, Cooperative grain boundary sliding in nanocrystalline materials, Phil. Mag. 86 (2006) 5797–5804.
[64] E. Ma, T.D. Shen, X.L. Wu, Nanostructured metals: less is more, Nat. Mater. 5 (2006) 515–516.
[65] Th Hentschel, D. Isheim, R. Kirchheim, F. Nuller, H. Kreye, Nanocrystalline Ni–3.6 at.% P and its transformation sequence studied by atom-probe field-ion microscopy, Acta Mater. 48 (2000) 933–941.
[66] A.J. Detor, M.K. Miller, C.A. Schuh, Solute distribution in nanocrystalline Ni-W alloys examined through atom probe topography, Phil. Mag. 86 (2006) 4459–4475.
[67] G.J. Fan, H. Choo, P.K. Liaw, Embrittlement in a bulk nanocrystalline alloy induced by room-temperature aging, Appl. Phys. Lett. 89 (2006), 061919.
[68] S.X. Li, G.R. Cui, Dependence of strength, elongation, and toughness on grain size in metallic structural materials, J. Appl. Phys. 101 (2007), 083525.
[69] H. Van Swygenhoven, P.M. Derlet, Grain-boundary sliding in nanocrystalline fcc metals, Phys. Rev. B 64 (2001), 224105.
[70] H.-H. Fu, D.J. Benson, M.A. Meyers, Analytical and computational description of effect of grain size on yield strength of metals, Acta Mater. 49 (2001) 2567–2582.
[71] M.Y. Gutkin, I.A. Ovid'ko, N.V. Skiba, Crossover from grain boundary sliding to rotational deformation in nanocrystalline materials, Acta Mater. 51 (2003) 4059–4071.

[72] J. Markmann, P. Bunzel, H. Rosner, K.W. Liu, K.A. Padmanabhan, R. Birringer, H. Gleiter, J. Weissmuller, Microstructure evolution during rolling of inert-gas condensed palladium, Scr. Mater. 49 (2003) 637–644.
[73] J. Schioz, K.W. Jacobsen, A maximum in the strength of nanocrystalline copper, Nature 301 (2003) 1357–1359.
[74] V. Yamakov, D. Wolf, S.R. Phillpot, A.K. Mukherjee, H. Gleiter, Deformation-mechanism map for nanocrystalline metals by molecular-dynamics simulation, Nat. Mater. 3 (2004) 43–47.
[75] J. Monk, D. Farkas, Strain-induced grain growth and rotation in nickel nanowires, Phys. Rev.B 75 (2007), 45414.
[76] M. Jin, A.M. Minor, E.A. Stach, J.W. Morris Jr., Direct observation of deformation-induced grain growth during the nanoindentation of ultrafine-grained Al at room temperature, Acta Mater. 52 (2004) 5381–5387.
[77] Z.W. Shan, E.A. Stach, J.M.K. Wiezorek, J.A. Knapp, D.M. Follstaedt, S.X. Mao, Grain boundary-mediated plasticity in nanocrystalline nickel, Science 305 (2004) 654–657.
[78] Y.B. Wang, B.Q. Li, M.L. Sui, S.X. Mao, Deformation-induced grain rotation and growth in nanocrystalline Ni, Appl. Phys. Lett. 92 (2008), 011903.
[79] M. Upmanyu, D.J. Srolovitz, A.E. Lobkovsky, J.A. Warren, W.C. Carter, Simultaneous grain boundary migration and grain rotation, Acta Mater. 54 (2006) 1707–1719.
[80] K. Zhang, J.R. Weertman, J.A. Eastman, Rapid stress-driven grain coarsening in nanocrystalline Cu at ambient and cryogenic temperatures, Appl. Phys. Lett. 87 (2005), 061921.
[81] D.S. Gianola, S. Van Petegem, M. Legros, S. Brandstetter, H. Van Swygenhoven, K. J. Hemker, Stress-assisted discontinuous grain growth and its effect on the deformation behavior of nanocrystalline aluminum thin films, Acta Mater. 54 (2006) 2253–2263.
[82] M. Legros, D.S. Gianola, K.J. Hemker, In situ TEM observations of fast grain-boundary motion in stressed nanocrystalline aluminum films, Acta Mater. 56 (2008) 3380–3393.
[83] T.J. Rupert, D.S. Gianola, Y. Gan, K.J. Hemker, Experimental observations of stress-driven grain boundary migration, Science 326 (2009) 1686–1690.
[84] D. Moldovan, D. Wolf, S.R. Phillpot, Theory of diffusion-accommodated grain rotation in columnar polycrystalline microstructures, Acta Mater. 49 (2001) 3521–3532.
[85] A.V. Sergueeva, N.A. Mara, A.K. Mukherjee, Grain boundary sliding in nanomaterials at elevated temperatures, J. Mater. Sci. 42 (2007) 1433–1438.
[86] K.S. Kumar, S. Suresh, M.F. Chisholm, J.A. Horton, P. Wang, Deformation of electrodeposited nanocrystalline nickel, Acta Mater. 51 (2003) 387–405.
[87] X.Z. Liao, F. Zhou, E.J. Lavernia, S.G. Srinivasan, M.I. Baskes, D.W. He, Y.T. Zhu, Deformation mechanism in nanocrystalline Al: partial dislocation slip, Appl. Phys. Lett. 83 (2003) 632–634.
[88] Y.T. Zhu, X.Z. Liao, X.L. Wu, Deformation twinning in nanocrystalline materials, Prog. Mater. Sci. 57 (2012) 1–62.
[89] J.W. Wang, S. Narayanan, J.Y. Huang, Z. Zhang, T. Zhu, S.X. Mao, Atomic-scale dynamic process of deformation-induced stacking fault tetrahedra in gold nanocrystals, Nat. Commun. 4 (2013) 2340.
[90] S. Cheng, Y.H. Zhao, Y. Guo, Y. Li, Q. Wei, X.L. Wang, Y. Ren, P.K. Liaw, H. Choo, E.J. Lavernia, High plasticity and substantial deformation in nanocrystalline NiFe alloys under dynamic loading, Adv. Mater. 21 (2009) 5001–5004.
[91] X.Z. Liao, A.R. Kilmanetov, R.Z. Valiev, H.S. Gao, X.D. Li, A.K. Mukherjee, J. F. Bingert, Y.T. Zhu, High-pressure torsion-induced grain growth in electrodeposited nanocrystalline Ni, Appl. Phys. Lett. 88 (2006), 021909.
[92] S. Cheng, Y.H. Zhao, Y.M. Wang, Y. Li, X.- Li Wang, P.K. Liaw, E.J. Lavernia, Structure modulation driven by cyclic deformation in nanocrystalline NiFe, Phys. Rev. Lett. 104 (2010) 255501.
[93] Y.B. Wang, J.C. Ho, Y. Cao, Dislocation density evolution during high pressure torsion of a nanocrystalline Ni-Fe alloy, Appl. Phys. Lett. 94 (2009), 091911.
[94] R.Z. Valiev, Y. Estrin, Z. Horita, T.G. Langdon, M.J. Zehetbauer, Y.T. Zhu, Producing bulk ultrafine-grained materials by severe plastic deformation: ten years later, J. Occup. Med. 68 (2016) 1216–1226.
[95] F.R.N. Nabarro, Report of a Conference on Strength of Solids, The Physical Society, London, England, 1948, p. 75.
[96] T.G. Langdon, An evaluation of the strain contributed by grain boundary sliding in superplasticity, Mater. Sci. Eng. A 174 (1994) 225–230.
[97] H. Hahn, K.A. Padmanabhan, A model for the deformation of nanocrystalline materials, Philos. Mag. B 76 (1997) 559–571.
[98] A. Hasnaoui, H. Van Swygenhoven, P.M. Derlet, Cooperative processes during plastic deformation in nanocrystalline fcc metals: a molecular dynamics simulation, Phys. Rev. B 66 (2002), 184112.
[99] S. Cheng, E. Ma, Y.M. Wang, L.J. Kecskes, K.M. Youssef, C.C. Koch, U. P. Trociewitz, K. Han, Tensile properties of in situ consolidated nanocrystalline Cu, Acta Mater. 53 (2005) 1521–1533.
[100] D. Jia, K.T. Ramesh, E. Ma, Effects of nanocrystalline and ultrafine grain sizes on constitutive behavior and shear bands in iron, Acta Mater. 51 (2003) 3495–3509.
[101] A. Korbel, P. Martin, Microscopic versus macroscopic aspect of shear bands deformation, Acta Metall. 34 (1986) 1905–1909.
[102] A. Korbel, The model of microshear banding in metals, Scr. Metall. Mater. 24 (1990) 1229–1231.